Supplementary Information

Dopant-free donor–acceptor type semi-crystalline polymeric hole transporting material for superdurable perovskite solar cells

Dong Won Kim[a], Min-Woo Choi[a], Won Sik Yoon[a], Seung Hwa Hong[a], Sungjin Park[a], Ji Eon Kwon[a,b] and Soo Young Park[,a]*

[a] Center for Supramolecular Optoelectronic Materials, Department of Materials Science and Engineering, Seoul National University, 1 Gwanak-ro, Gwanak-gu, Seoul 08826, South Korea.

E-mail: parksy@snu.ac.kr

[b] (Present address) Functional Composite Materials Research Center Institute of Advanced Composite Materials, Korea Institute of Science and Technology (KIST), Jeonbuk 55324, South Korea.

Experimental details

Materials: Indium tin oxide glass substrate with a sheet resistance of 15 Ω sq^{-1} were purchased from AMG tech (Korea). Spiro-OMeTAD (99.5%, Lumtech), PbI_2 (99.999%, Sigma Aldrich), $PbBr_2$ (99.999%, Alfa Aesar), CsI (99.999%, Sigma-Aldrich), 2-(4-fluorophenyl)ethylamine hydroiodide (TCI), dimethyl sulfoxide (99.8%, Sigma Aldrich), *N*, *N*-dimethylformamide (99.8%, Sigma Aldrich), diethyl ether (99.7%, Sigma Aldrich), chlorobenzene (99.8% Sigma Aldrich), chloroform (99% Sigma Aldrich), hydriodic acid (HI, 57 wt% in H_2O, Sigma-Aldrich), hydrobromic acid (48 wt% in water), methylamine solution (40 wt%, TCI) and formamidine acetate (99%, Sigma-Aldrich) were purchased. All chemicals were used as received.

Synthesis of perovskite precursors: For methylammonium iodide (MAI), 27 mL of HI was reacted with 30 mL of methylamine solution in a 250 mL round-bottom flask. After stirring for 2 h, white precipitate was formed and collected by evaporating solvent at 65 ℃ using rotary evaporator. The solid precipitate was dissolved in ethanol and recrystallized with diethyl ether. The white powder was filtered and dried under vacuum for 24 h. For formamidinium iodide (FAI), 30 mL of HI was reacted with 20 g of formamidinium acetate in a 250 mL round-bottom flask. Dark yellow precipitate was formed. The powder collection and purification process are the same with MAI synthesis procedure. For methylammonium bromide (MABr), 30 mL of HBr was reacted with 33 mL of methylamine solution in a 250 mL round-bottom flask. Dark brown powder was precipitated. The powder collection and purification process are the same with MAI synthesis procedure.

Perovskite solar cell device fabrications: The patterned indium tin oxide (ITO) glass substrates were wet-cleaned in an ultrasonic bath of deionized water, acetone, and isopropanol for each 20 min. After an ultraviolet-ozone treatment for 30 min, the 3 wt% SnO_2 aqueous colloidal solution, prepared by diluting 15 wt% SnO_2 colloidal solution (Alfa aesar) dissolved in water, was spin-coated on patterned ITO glass substrate at 5,000 rpm for 50 s and then annealed at 150 ℃ for 30 min. For $MAPbI_3$ layer, a 50 wt% perovskite solution was prepared by PbI_2:MAI (1:1 molar ratio) in DMF:DMSO (0.89:0.11 v/v). During spin coating process, 0.3 ml of diethyl ether was dropped on substrate and annealed at 65 ℃ for 1 min and at 100 ℃ for 2 min. For $Cs_{0.05}FA_{0.90}MA_{0.05}PbI_{2.85}Br_{0.15}$ layer, a 47 wt% perovskite solution was prepared by dissolving PbI_2, $PbBr_2$, FAI, MABr, and CsI in DMF and DMSO (0.8:0.2 v/v). The solution was spin-coated at 5000 rpm for 25 s. During spin coating process, 0.3 ml of chlorobenzene was dropped on substrate and annealed at 150 ℃ for 15 min. 50 ul of 4-fluoro-phenylethylammonium iodide (15 mM in IPA) was spin-coated on the perovskite film at 5,000 rpm for 20 s. The Spiro-

OMeTAD solution (72 mg/ml in chlorobenzene) with 28.8 μL of 4-*t*BP and 17.5 μL (520 mg/ml in acetonitrile) was spin-coated on the perovskite layer at 6000 rpm for 20 s. In the case of polymer HTM, 110−120 nm films of NTDT-based polymers were spin coated on top of perovskite layer. All thicknesses have an error of 10 nm. Finally, 80 nm of gold electrode was deposited by thermal evaporation under a vacuum of 10^{-6} Torr.

Instruments and Characterization: AFM images of polymer films were obtained in tapping mode with a NX-10 (Park Systems, Korea). UV-vis absorption spectra of polymer solution were measured using a SHIMADZU UV-1650PC. Photoluminescence quenching spectra of samples (quartz/ perovskite and quartz/ perovskite/ polymer HTMs) were obtained with a PTI QuantaMaster 40 spectrofluorometer. Photoluminescence decay traces were obtained through the time correlated single photon counting techniques by using a PicoQuant, FluoTime 250 instrument (Germany) and the film samples were excited with a 377 nm pulsed laser. Water contact angles were measured using DSA 100L (Krüss). The thickness of polymer films was measured using a surface profiler ET200 (KOSAKA). The cross-sectional scanning electron microscope (SEM) image were obtained by using MERLIN Compact (ZEISS). Depth profiling of device was analyzed by time-of-flight secondary ion mass spectrometry (ToF-SIMS) using ToF-SIMS-5 instrument (ION-TOF) quipped with a 25 KeV bismuth(Bi) primary ion-source.

GIWAXS measurement: Grazing incidence X-ray diffraction (GIXRD) measurements were performed at the PLS-II 9A U-SAXS beamline in the Pohang Accelerator Laboratory, Pohang, Republic of Korea. For the analysis of device stored at humid condition (90 ± 5 RH), the X-ray incidence angle was adjusted to 0.13~0.16° for obtaining the information in the depth direction.

SCLC measurement: For space-charge-limited currents (SCLC) measurement, hole-only devices were fabricated with the configuration of ITO/PEDOT:PSS (40 nm)/polymer HTM (~150 nm)/Au (80 nm). The hole mobility was determined by using dark current under forward bias. The SCLC mobilities were calculated using the below equation:

$$J = \frac{9}{8}\varepsilon_r\varepsilon_0\mu_0\frac{V^2}{L^3}$$

where J is the current density, ε_r is the dielectric constant of the polymer (dielectric constant assumed to be 3), ε_0 is the permittivity of free space, μ_0 is the zero-field hole mobility, L is the polymer thickness, and the effective voltage, $V = V_{appl} - V_{bi}$, where V_{appl} is the applied voltage to the device, and V_{bi} is the built-in voltage. The hole mobility was calculated from the slope ($J \sim V^2$).

Device characterization: The current density (J)–voltage (V) characteristics of PSCs were measured by using a Keithley 4200 source measurement unit. The solar cell performances were characterized AM 1.5G conditions with an illumination intensity of 100 mW cm^{-2}, as generated by an Oriel Sol3A solar simulator. The lamp irradiation was calibrated using a NREL certificated KG-5 filtered standard silicon photodiode (VLSI Standards Inc.). The active area was 0.05 cm^2 and measurements were carried out under an ambient atmosphere. The incident photon-to-current efficiency (IPCE) was measured using an Oriel QE/IPCE Measurement Kit comprised of a 300 W xenon lamp, a monochromator (74125), a Merlin lock-in amplifier (70104), an optical chopper, and a calibrated silicon photodiode (70356_70316NS).

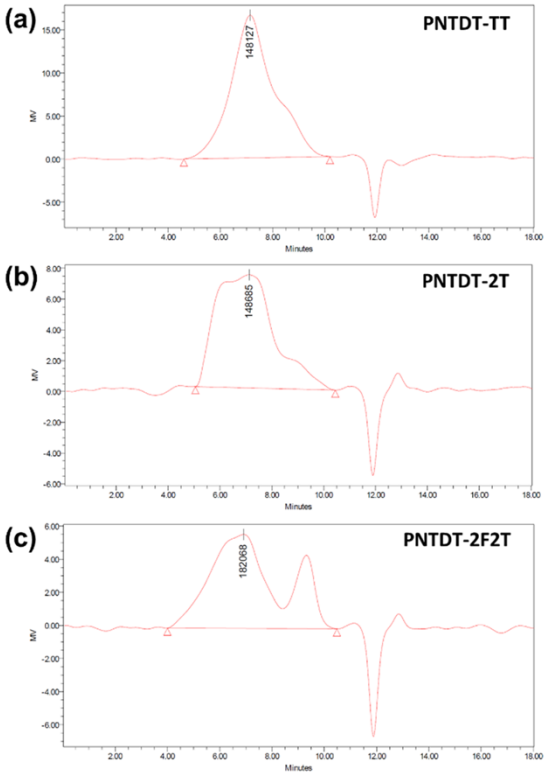

M_n (kDa)	M_w (kDa)	PDI
91	213	2.34

M_n (kDa)	M_w (kDa)	PDI
89	290	3.25

M_n (kDa)	M_w (kDa)	PDI
60	850	14.16

Figure S1. GPC curves of a) PNTDT-TT, b) PNTDT-2T, and c) PNTDT-2F2T.

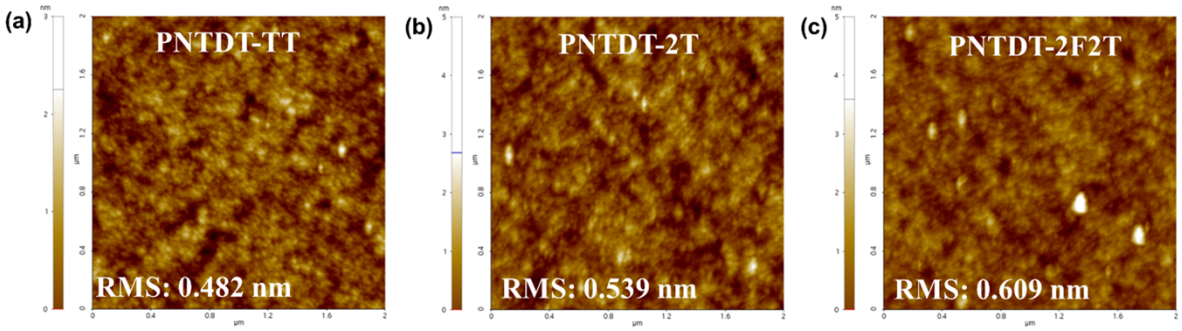

Figure S2. AFM height images (2 × 2 μm) of the a) PNTDT-TT, b) PNTDT-2T, and c) PNTDT-2F2T films.

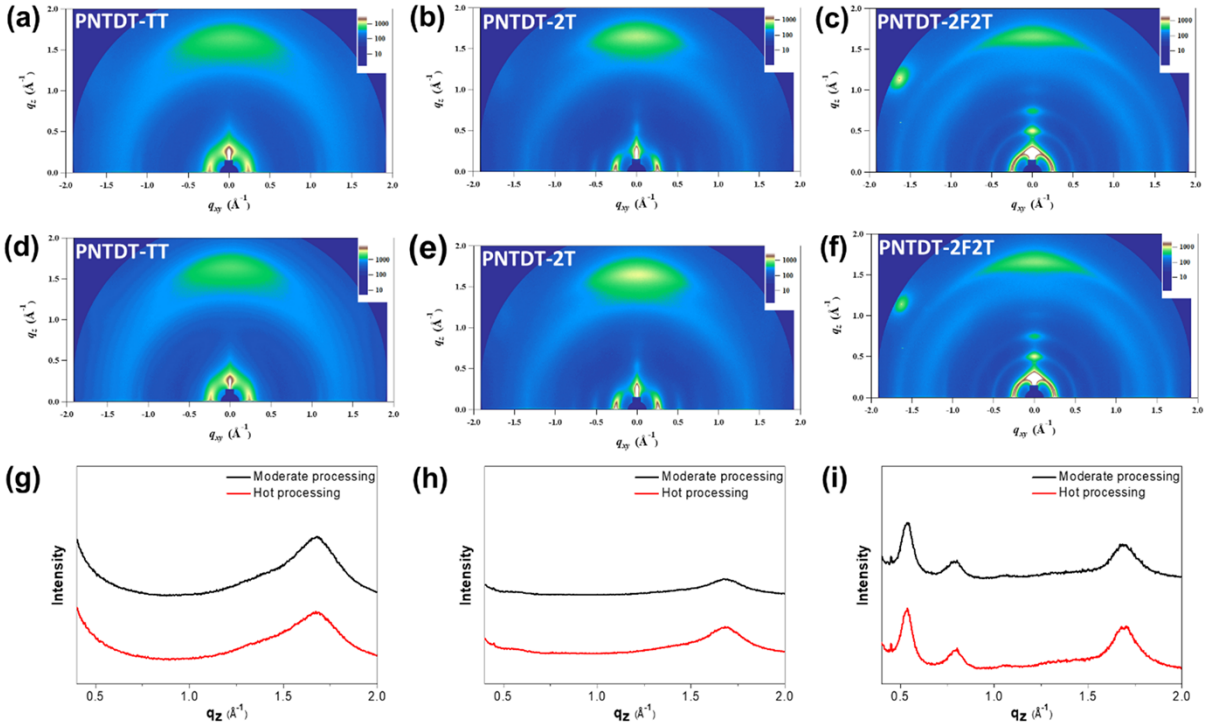

Figure S3. GIWAXS images of a) PNTDT-TT, b) PNTDT-2T, and c) PNTDT-2F2T films coated on SiO_2 substrate by moderate processing. GIWAXS images of d) PNTDT-TT, e) PNTDT-2T, and f) PNTDT-2F2T films coated on SiO_2 by hot processing. Out-of-plane line cut profiles of g) PNTDT-TT, h) PNTDT-2T, and i) PNTDT-2F2T films.

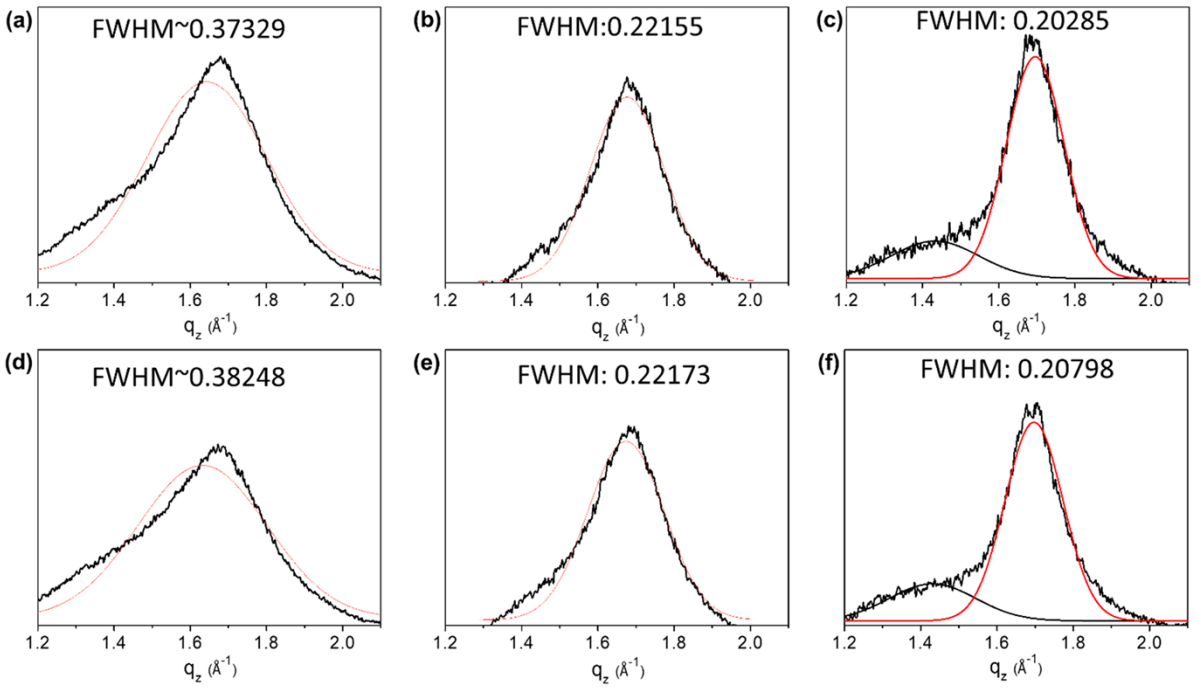

Figure S4. The full width at half maximum of (010) peaks of a) PNTDT-TT, b) PNTDT-2T, and c) PNTDT-2F2T films coated on SiO_2 by moderate processing. The full width at half maximum of (010) peaks of d) PNTDT-TT, e) PNTDT-2T, and f) PNTDT-2F2T films coated on SiO_2 by hot processing.

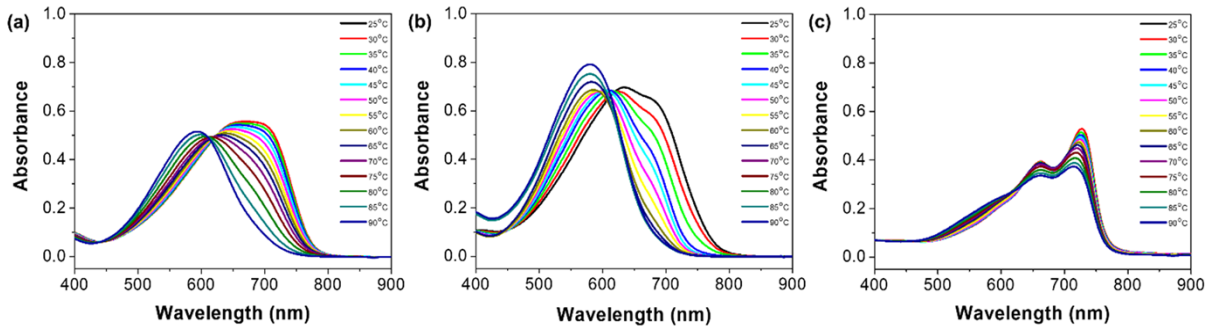

Figure S5. Ultraviolet-visible absorption spectra of a) PNTDT-TT, b) PNTDT-2T, and c) PNTDT-2F2T in chlorobenzene solution at various temperatures.

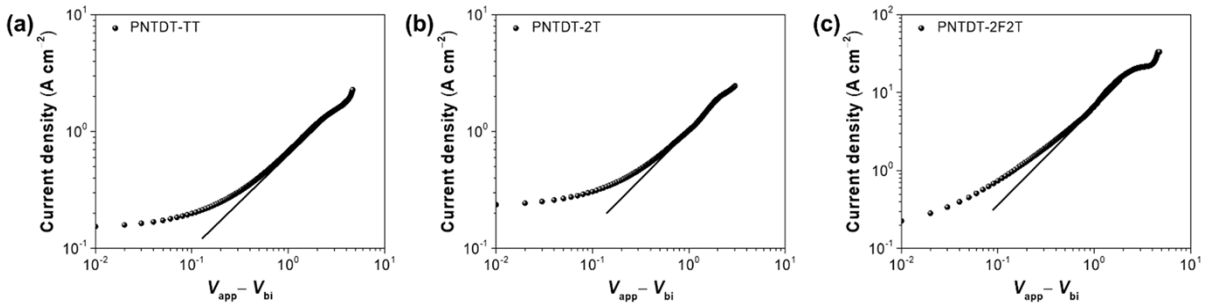

Figure S6. The dark $J-V$ curves of hole-only device with the structure of ITO/PEDOT:PSS/HTM/Au. HTM: a) PNTDT-TT, b) PNTDT-2T, and c) PNTDT-2F2T.

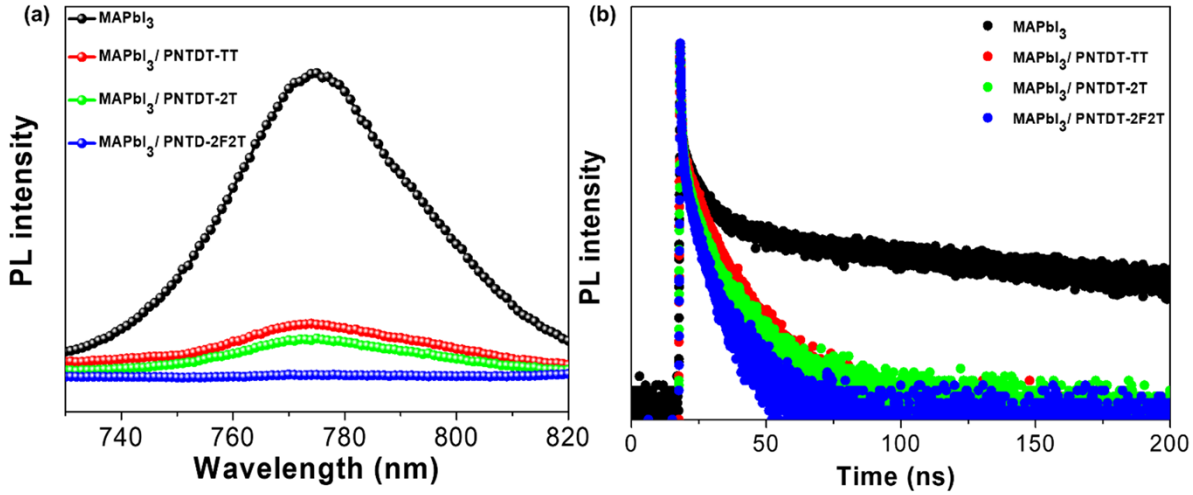

Figure S7. a) PL emission curves of bare $MAPbI_3$ and NTDT-based polymers coated on $MAPbI_3$. b) Time-resolved PL decay curves of bare $MAPbI_3$ and NTDT-based polymers coated on $MAPbI_3$.

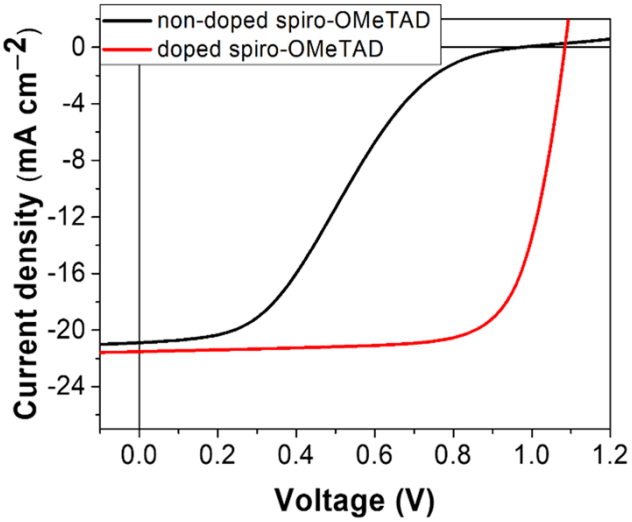

Figure S8. $J-V$ curves of $MAPbI_3$-based PSC devices with non-doped and doped spiro-OMeTAD.

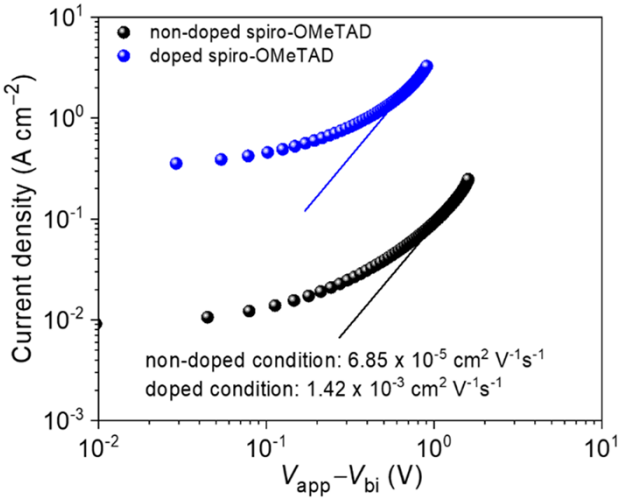

Figure S9. The dark $J-V$ curves of spiro-OMeTAD-based hole-only devices and their hole mobilities in non-doped and doped condition.

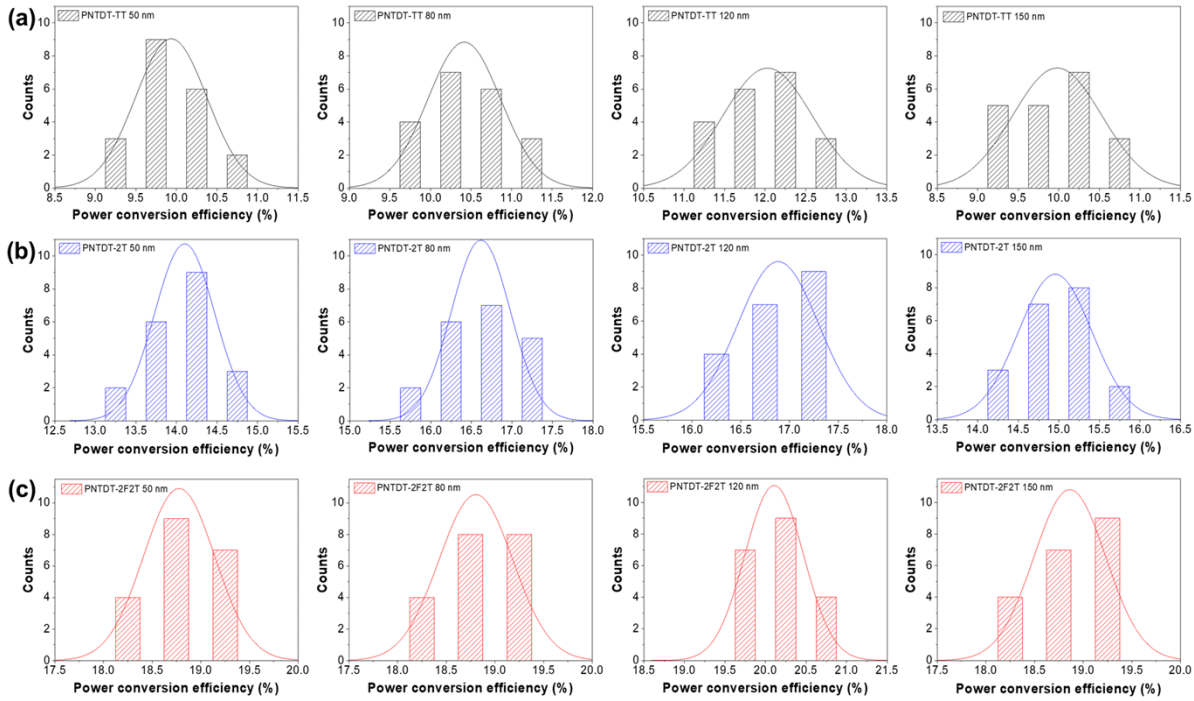

Figure S10. Statistical PCE values of the $MAPbI_3$-based PSC devices employing a) PNTDT-TT, b) PNTDT-2T and c) PNTDT-2F2T applied at various thickness.

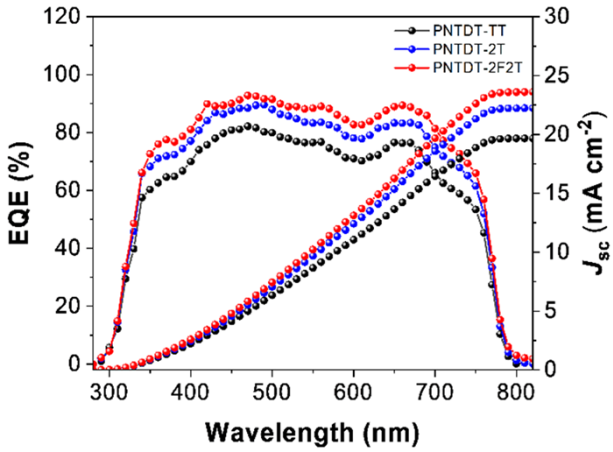

Figure S11. IPCE curves of $MAPbI_3$-based perovskite solar cells with NTDT-based polymers.

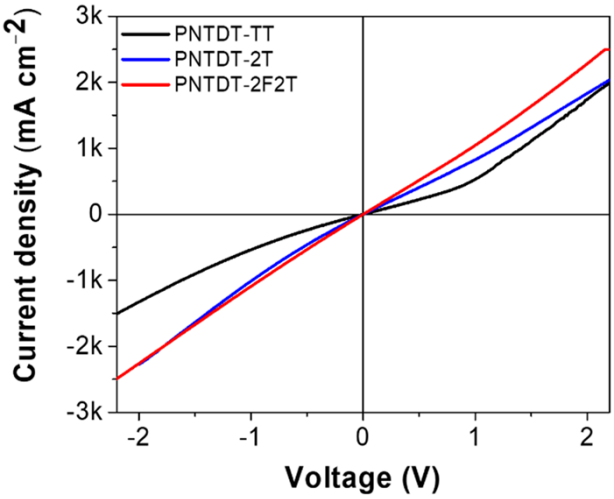

Figure S12. *J*−*V* curves of hole-only devices with a structure of ITO/PEDOT:PSS/HTM/Au.

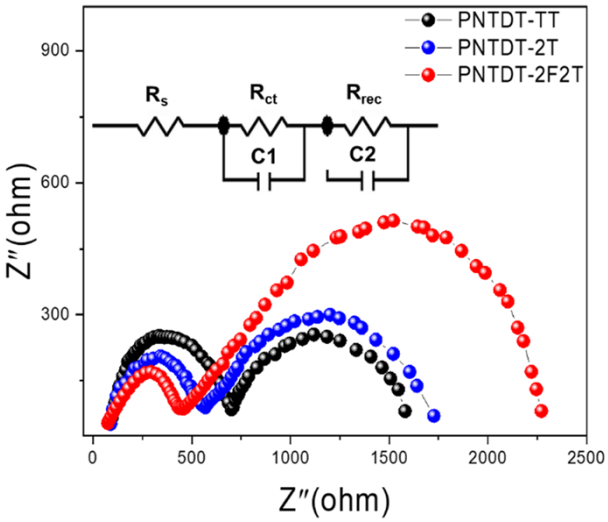

Figure S13. Electrical impedance spectroscopy spectra of the devices with NTDT based polymers.

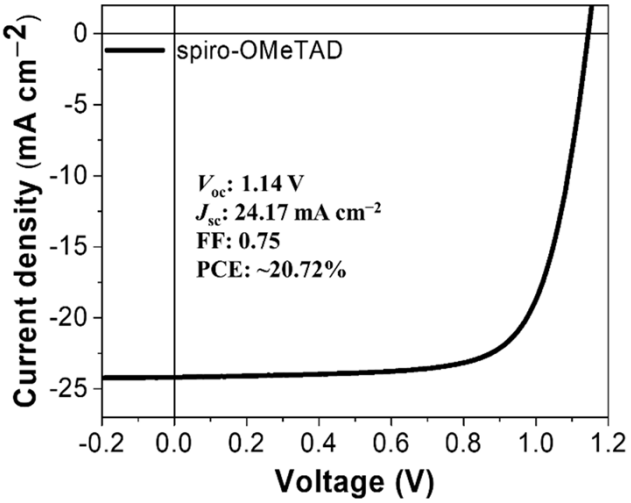

Figure S14. *J*–*V* curve of $Cs_{0.05}FA_{0.90}MA_{0.05}PbI_{2.85}Br_{0.15}$-based the PSC device with doped spiro-OMeTAD.

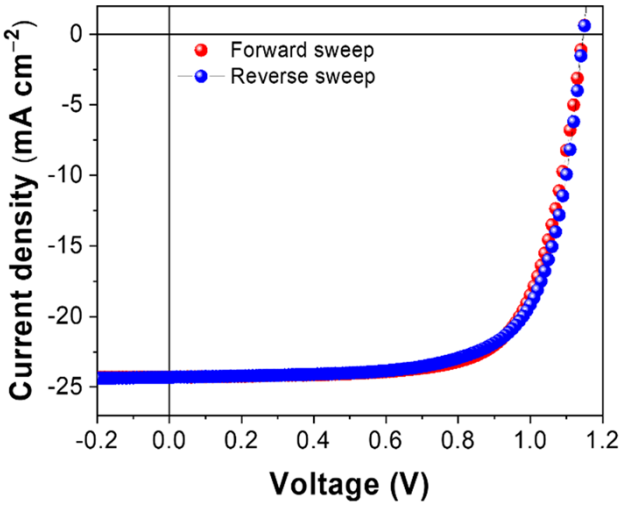

Figure S15. *J*–*V* curves of $Cs_{0.05}FA_{0.90}MA_{0.05}PbI_{2.85}Br_{0.15}$-based the PSC device with PNTDT-2F2T measured by forward (− 0.2 V → 1.4 V) and reverse (1.4 V → − 0.2 V) sweeps.

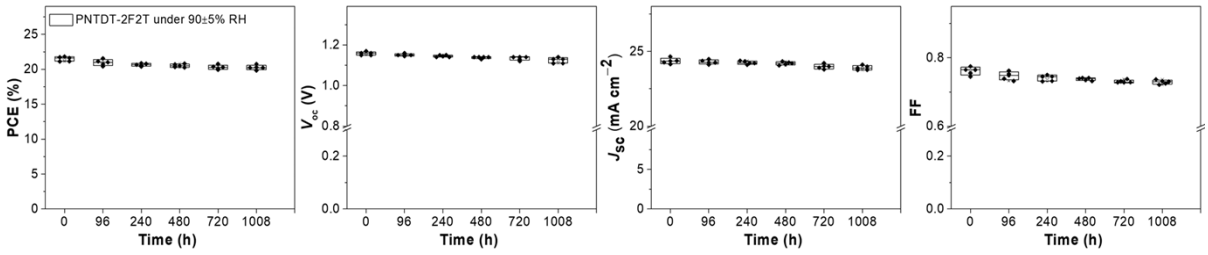

Figure S16. Trace of the long-term efficiency of $Cs_{0.05}FA_{0.90}MA_{0.05}PbI_{2.85}Br_{0.15}$-based PSC devices employing PNTDT-2F2T under 90 ± 5% RH.

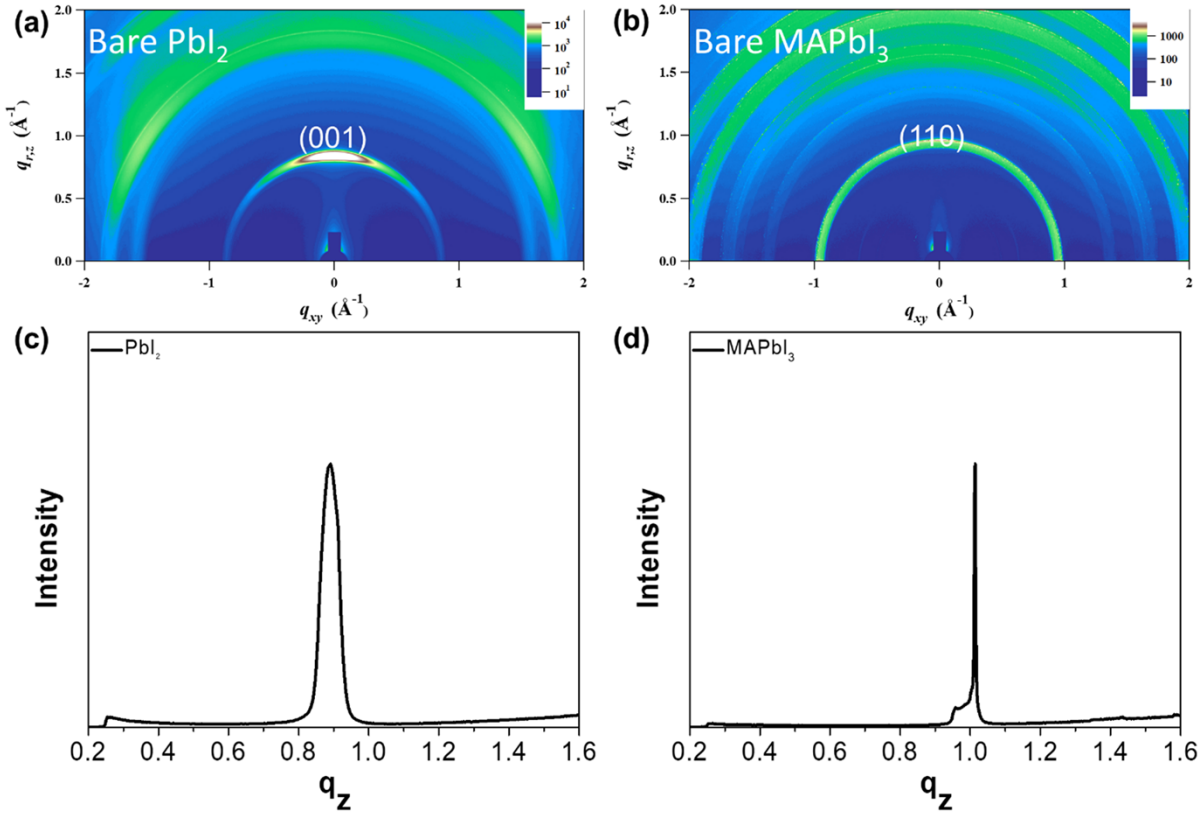

Figure S17. GIWAXS images of a) PbI_2 and b) $MAPbI_3$ films. Out-of-plane line cut profiles of c) PbI_2 and d) $MAPbI_3$ films.

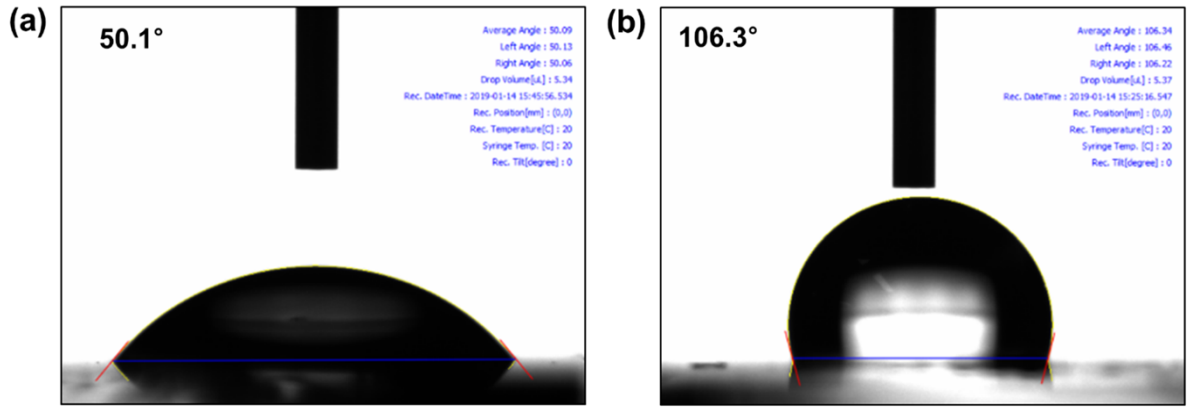

Figure S18. Water contact angles of a) doped spiro-OMeTAD film and b) PNTDT-2F2T film.

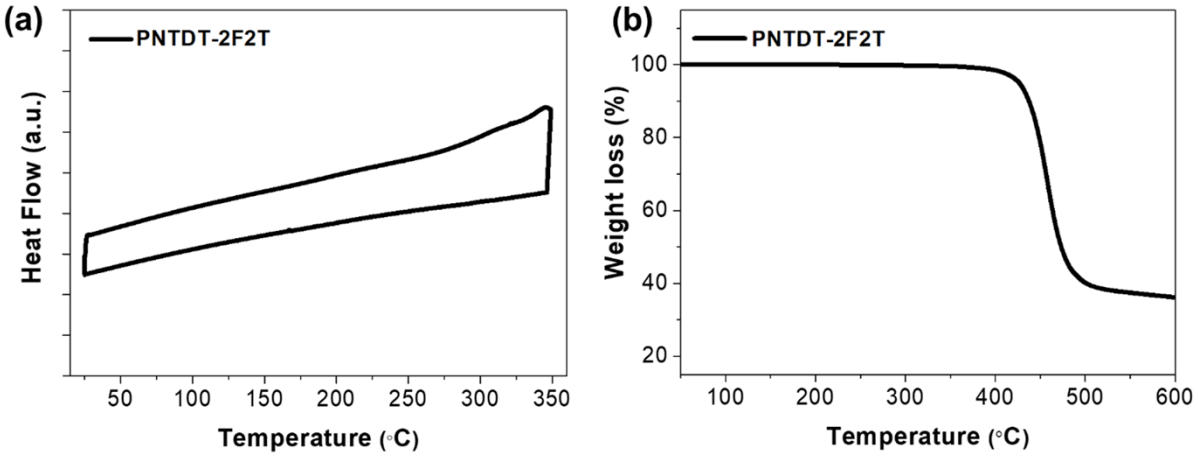

Figure S19. a) DSC curve and b) TGA curve of PNTDT-2F2T.

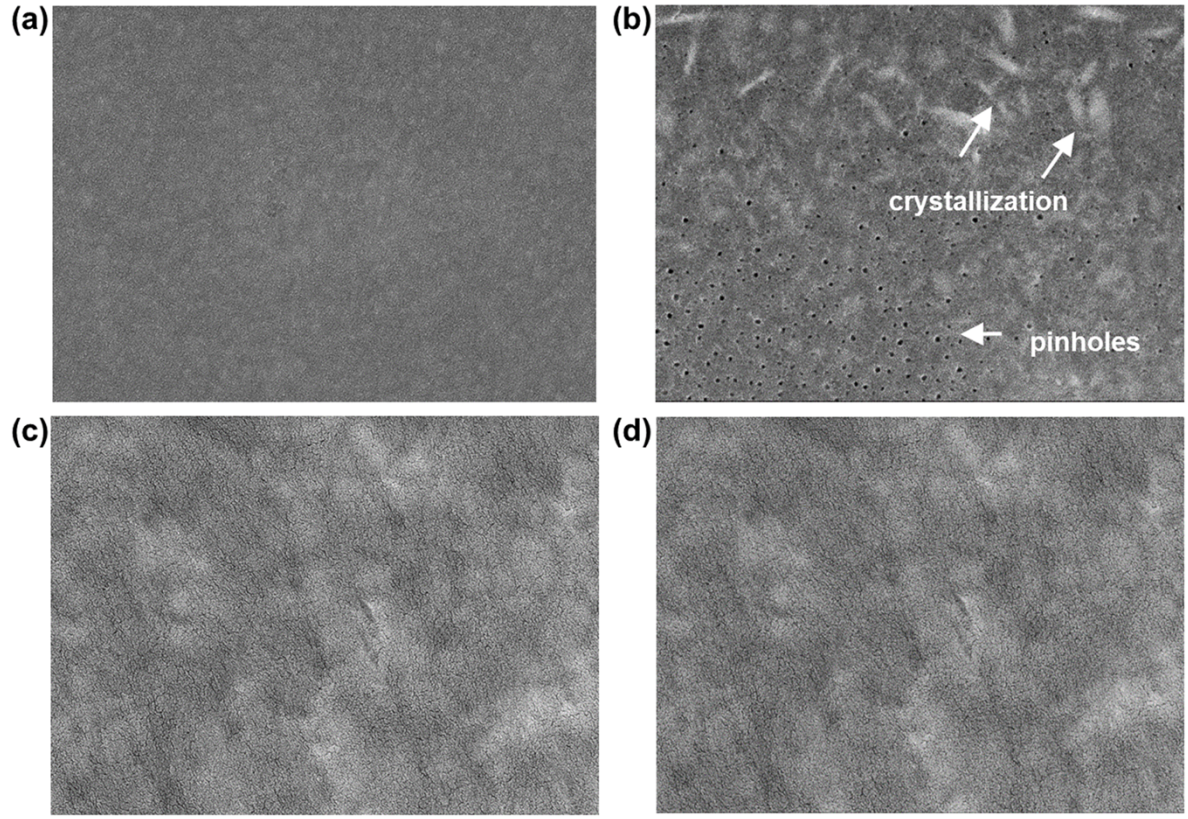

Figure S20. The top-view SEM image of spiro-OMeTAD layer of a) pristine device and b) 1008 h-thermally-aged device. The top-view SEM image of PNTDT-2F2T layer of c) pristine device and d) 1008 h-thermally-aged device.

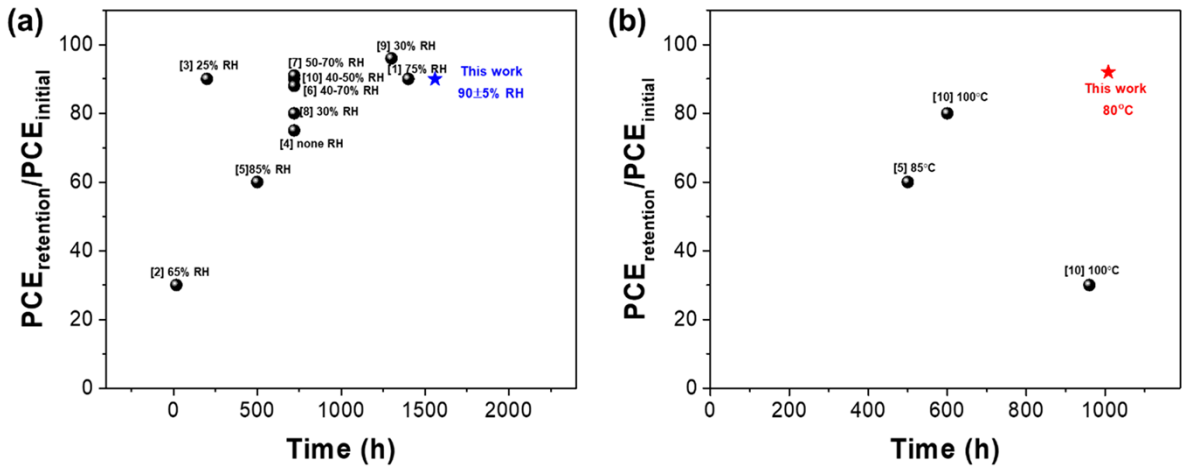

Figure S21. The comparison of long-term durability of PSC devices using D–A type polymer under a) constant humidity and b) thermal annealing, respectively.

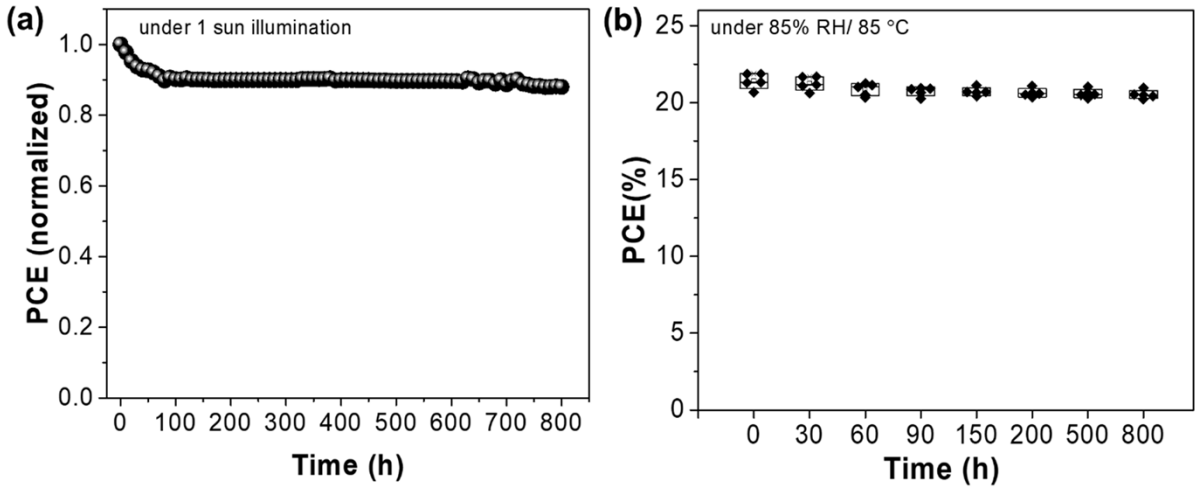

Figure S22. a) Operational stability of PSC device with PNTDT-2F2T under nitrogen (N_2) atmosphere. The stability was measured under maximum power point tracking and continuous light illumination (100 mW cm^{-2}) without a UV cut-off filter. b) Damp heat stability of encapsulated PSC devices with PNTDT-2F2T under 85% RH/ 85 ℃ condition.

Table S1. Comparison of performance and stability of D–A type polymer HTMs.

Material	Mobility [$cm^2 V^{-1} s^{-1}$]	Thickness [nm]	Stability	Stability condition	Initial PCE [%]	PCE retention rate (Time, hour)	Ref
RCP	3.34×10^{-3}	N.D.	M	75% RH	17.30	over 90% (1400 h)	[1]
pBBTa-BDT2	2×10^{-3}	50	M	65% RH, 85 ℃	14.50	30% (18 h)	[2]
PTEG	1.64×10^{-3}	100	M	25% RH	19.80	over 90% (200 h)	[3]
P2-2F	9.32×10^{-5}	N.D.	M	-	14.94	75% (720 h)	[4]
PPDT2FBT	7.3×10^{-3}	50	M, T, P	85% RH, 85 ℃, 1 sun	16.8	60% (500 h)	[5]
PCDTBT1	1×10^{-3}	20	M	40−70% RH (Encapsulation)	19.10	90% (720 h)	[6]
asy-PBTBDT	1.13×10^{-3}	N.D.	M	50−70% RH, 25 ℃	18.3	91% (720 h)	[7]
PBDTT	7.16×10^{-4}	50	M	30% RH, 25 ℃	20.28	80% (720 h)	[8]
PDTPC-1	3.98×10^{-3}	N.D.	M	30% RH	16.96	96% (1300 h)	[9]
alkoxy-PTEG	4.06×10^{-4}	30	M	40−50% RH	21.2	88% (720 h)	[10]
			T	100 ℃	-	80% (600 h) 30% (960 h)	
PffBT4T-2OD	N.D.	N.D.	-	-	17.6	-	[11]
PNTDT-2F2T	2.14×10^{-2}	120	M	90 ± 5% RH, 25 ℃	20.60 ($MAPbI_3$) 22.19% (Mixed perovskite)	90% (1560 h) 92% (1008 h)	This work
			T	80 ℃, N_2	22.19% (Mixed perovskite)	85% (1008 h)	
			M, T	85% RH, 85 ℃ (Encapsulation)		95% (800 h)	
			P	1 sun MPP tracking, N_2		88% (800h)	

M: moisture stability, T: thermal stability, and P: photostability

Table S2. The π–π distance and crystal coherence length of NTDT-based polymer films prepared by moderate and hot processing.

Polymer film	Moderate processing			Hot processing		
	q_z ($Å^{-1}$)	π–π stack (Å)	CCL (Å)	q_z ($Å^{-1}$)	π–π stack (Å)	CCL (Å)
PNTDT-TT	1.6813	3.74	16.83	1.6830	3.73	16.43
PNTDT-2T	1.6865	3.73	28.36	1.6847	3.72	28.34
PNTDT-2F2T	1.7124	3.67	30.97	1.7108	3.67	30.21

Table S3. SCLC hole mobility of NTDT-based polymers (ITO/PEDOT/Polymer/Au).

Material	SCLC hole mobility [$cm^2\ V^{-1}\ s^{-1}$]
PNTDT-TT	2.30×10^{-3}
PNTDT-2T	4.91×10^{-3}
PNTDT-2F2T	2.14×10^{-2}

Table S4. Summary of components related to lifetime extracting from TR-PL curves of bare $MAPbI_3$ and $MAPbI_3$/NTDT-based polymer.

Samples	A1 (%)	τ_1 (ns)	A2 (%)	τ_2 (ns)	τ_{ave} (ns)
$MAPbI_3$	3	1.1	97	366.7	366.4
$MAPbI_3$/PNTDT-TT	26.3	29.2	73.7	36.0	34.5
$MAPbI_3$/PNTDT-2T	42.1	27.3	57.9	36.5	33.3
$MAPbI_3$/PNTDT-2F2T	59.1	24.6	40.9	37.5	31.4

Table S5. Photovoltaic parameters of the $MAPbI_3$-based PSC devices using non-doped and doped spiro-OMeTAD.

Condition	V_{oc} (V)	J_{sc} (mA cm^{-2})	FF	PCE (%)
Pristine	0.97	20.39	0.30	6.34
Doped	1.08	21.52	0.74	17.26

Table S6. Photovoltaic performance of PSCs with NTDT-based polymers of different thicknesses.

HTM	Thickness [nm]	V_{oc} [V]	J_{sc} [mA cm^{-2}]	FF	PCE [%]
PNTDT-TT	~50	1.02	18.24	0.58	10.82
	~80	1.01	18.41	0.60	11.18
	~120	1.05	19.68	0.62	12.88
	~150	1.05	17.87	0.58	10.92
PNTDT-2T	~50	1.02	22.01	0.65	14.62
	~80	1.10	22.62	0.68	17.04
	~120	1.10	22.65	0.70	17.49
	~150	1.06	22.29	0.65	15.55
PNTDT-2F2T	~50	1.08	23.62	0.75	19.15
	~80	1.10	23.74	0.74	19.35
	~120	1.13	24.02	0.75	20.60
	~150	1.10	24.21	0.72	19.21

Table S7. Summaries of resistance obtained from electrical impedance spectroscopy for the devices with NTDT-based polymers.

Sample	R_{ct} (Ω)	R_{rec} (Ω)
PNTDT-TT	609.98	790.12
PNTDT-2T	480.11	1069.77
PNTDT-2F2T	362.68	1760.50

References

[1] G.-W. Kim, G. Kang, J. Kim, G.-Y. Lee, H. I. Kim, L. Pyeon, J. Lee, T. Park, *Energy Environ. Sci.* **2016**, *9*, 2326.

[2] H.-C. Liao, T. L. D. Tam, P. Guo, Y. Wu, E. F. Manley, W. Huang, N. Zhou, C. M. M. Soe, B. Wang, M. R. Wasielewski, L. X. Chen, M. G. Kanatzidis, A. Facchetti, R. P. H. Chang, T. J. Marks, *Adv. Energy Mater.* **2016**, *6*, 1600502.

[3] G.-W. Kim, J. Lee, G. Kang, T. Kim, T. Park, *Adv. Energy Mater.* **2018**, *8*, 1701935.

[4] K. Kranthiraja, S. H. Park, H. Kim, K. Gunasekar, G. Han, B. J. Kim, C. S. Kim, S. Kim, H. Lee, R. Nishikubo, A. Saeki, S. H. Jin, M. Song, *ACS Appl. Mater. Interfaces* **2017**, *9*, 36053.

[5] C. W. Koh, J. H. Heo, M. A. Uddin, Y. W. Kwon, D. H. Choi, S. H. Im, H. Y. Woo, *ACS Appl. Mater. Interfaces* **2017**, *9*, 43846.

[6] F. Cai, J. Cai, L. Yang, W. Li, R. S. Gurney, H. Yi, A. Iraqi, D. Liu, T. Wang, *Nano Energy* **2018**, *45*, 28.

[7] J. Lee, M. Malekshahi Byranvand, G. Kang, S. Y. Son, S. Song, G. W. Kim, T. Park, *J. Am. Chem. Soc.* **2017**, *139*, 12175.

[8] G. You, Q. Zhuang, L. Wang, X. Lin, D. Zou, Z. Lin, H. Zhen, W. Zhuang, Q. Ling, *Adv. Energy Mater.* **2020**, *10*, 1903146.

[9] Z. Zhang, L. Liang, L. Deng, L. Ren, N. Zhao, J. Huang, Y. Yu, P. Gao, *ACS Appl. Mater. Interfaces* **2021**, *13*, 6688.

[10] J. Lee, G. W. Kim, M. Kim, S. A. Park, T. Park, *Adv. Energy Mater.* **2020**, *10*, 1902662.

[11] Y. Hou, X. Du, S. Scheiner, D. P. McMeekin, Z. Wang, N. Li, M. S. Killian, H. Chen, M. Richter, I. Levchuk, N. Schrenker, E. Spiecker, T. Stubhan, N. A. Luechinger, A. Hirsch, P. Schmuki, H.-P. Steinrück, R. H. Fink, M. Halik, H. J. Snaith, C. J. Brabec, *Science* **2017**, *358*, 1192.